RESEARCH ARTICLE

LASER & PHOTONICS REVIEWS

www.lpr-journal.org

Hybrid Femtosecond Laser 3D Processing Technology for Rapid Integration of Functional Optical Devices on Fibers

Liqun Xu, Yuhang Xue, Chaowei Wang, Xinyu Gui, Chenchu Zhang, Li Zhang, Yuan Tao, Xinghao Wang, Leran Zhang, Deng Pan, Jiawen Li, Dong Wu, Jiaru Chu, and Yanlei Hu**

Due to constraints imposed by the geometry characteristics of optical fibers and conventional preparation strategies, the development of "Lab on Tip" devices faces significant challenges. By introducing two-photon polymerization (TPP) technology, it becomes feasible to develop arbitrarily complex 3D structures with nanoscale features on fiber tips. However, the serial scanning process of TPP is too slow to accommodate the extensive application expansion of fiber tip devices. Herein, a hybrid femtosecond laser 3D processing technology (termed "FPL-DLW"), developed by combining femtosecond projection lithography (FPL) with direct laser writing (DLW), is reported. FPL is adopted to print bulk base structures and DLW is employed for precision realization of functional nanostructures. Using a common polarizing beam splitter as a bridge, the two independent optical systems with different polarized light sources are facilely integrated to realize hybrid processing. The FPL-DLW utilizes FPL (high-efficiency) and DLW (high-precision) to flexibly fabricate multiple types of fiber tip functional devices, whose processing efficiency can be boosted by up to two orders of magnitude compared to using DLW alone. These results validate that the authors' method provides a universal solution for the rapid integration of micro–nanostructures on various fiber end facets, which is challenging with existing TPP technologies.

1. Introduction

Since the invention of silica-based fiber, it has become one of the most extensive devices in the fields of communications, sensing, lasing, and imaging due to the extraordinary features of small size and low optical loss. The recent concept of "Lab on Fiber"[1] has opened up a new pathway to create fibers that are capable of visualizing, listening, perceiving, and communicating by incorporating different materials and structures with various functions into optical fiber configurations. Depending on the specific location where functional components are integrated, the "Lab on Fiber" can be categorized into three paradigms: "Lab in Fiber,"[2,3] "Lab around Fiber,"[4] and "Lab on Tip."[5–7] Among these, "Lab on Tip" devices, which integrate various functional devices on the end facet of fibers, have gained significant prominence as versatile, plug-and-play solutions for optical networks. These devices utilize the small and finely cleaved end of the fiber as their light-coupled platform, offering advantages of ultra-compact size, minimal insertion loss, and multifunctionality. However, the unconventional shape of the small cross-section and large aspect ratio of the fibers poses challenges when trying to devise appropriate strategies for fabrication on their tips.

To address these challenges, researchers have employed two main approaches: material transfer[8] and direct fabrication.[9] The former uses planar nanotechnologies to pre-fabricate nanostructures on a planar substrate; and then, transfers them onto the fiber tips. However, it is difficult to ensure that the structures can be intact, firmly bonded to the fiber end, and accurately aligned to the fiber core during the transfer process, which limits the performance of devices.[10] In contrast, the latter focuses on preparing microstructures directly on the microscale plane of the fiber end by optimized fabrication methods. However, direct modification of the fiber end at the macroscale results in rough surface and poor control of the final geometry. Alternatively, electron-beam lithography and focused ion beam milling techniques provide fabrication resolution in the deep subwavelength regime, nevertheless facing compelling challenges in handling arbitrary complex 3D structures.[11]

L. Xu, Y. Xue, C. Wang, X. Gui, L. Zhang, Y. Tao, X. Wang, L. Zhang, J. Li, D. Wu, J. Chu, Y. Hu
CAS Key Laboratory of Mechanical Behavior and Design of Materials
Department of Precision Machinery and Precision Instrumentation
University of Science and Technology of China
Hefei 230026, China
E-mail: chaoweiw@ustc.edu.cn; huyl@ustc.edu.cn

C. Zhang
Anhui Province Key Lab of Aerospace Structural Parts Forming Technology and Equipment
Institute of Industry & Equipment Technology
Hefei University of Technology
Hefei 230009, China

L. Zhang
Anhui Qingyu Photoelectric Technology Co., Ltd
Hefei 230088, China

D. Pan
Information Materials and Intelligent Sensing Laboratory of Anhui Province
Anhui University
Hefei 230601, China

The ORCID identification number(s) for the author(s) of this article can be found under https://doi.org/10.1002/lpor.202400708

DOI: 10.1002/lpor.202400708

Femtosecond laser two-photon polymerization (TPP) technology, with its high resolution (<100 nm) and true 3D processing capability, has been developed into an outstanding sub-micron additive manufacturing technology.[12–15] In recent years, the combination of TPP and the concept of "Lab on Tip" has not only fully exploited the advantages of fibers as an ultra-compact light-coupled platform but also led to the birth of a myriad of unprecedented fiber optical devices.[16–21] However, the most common implementation of TPP for printing "Lab on Tip" devices is through a serial scanning of the laser focus in the photosensitive polymer attached to the fiber end facet, which makes mass production impractical. To solve this problem, researchers spliced a sub-millimeter coreless fiber on a single-mode fiber (SMF) for beam expansion and effective reduction of printing volume.[22–24] This improvement measure is only applicable to the specific application scenario of preparing a single beam shaping element on SMF, and it requires additional configuration of an integrated fiber processing workstation. As an alterative, adopting parallelized TPP technology is a promising approach. However, it is still challenging to increase the manufacturing throughput without affecting the resolution or superior design flexibility. For example, microlens array[25] and diffractive optical element (DOE)[26] can be used to split a laser beam into multiple focal points for parallel printing, but the generated laser focal points cannot be controlled individually. Therefore, these methods cannot handle non-periodic freeform structures. The use of liquid crystal on silicon spatial light modulator (LCoS-SLM) allows for dynamic modulation of the laser beam, which can achieve flexibly independent control of each laser focal point, but the beam switching is limited by the low refresh rate of LCoS-SLM.[27,28] The emerging femtosecond projection TPP technology using a digital micromirror device (DMD) to dynamically generate complex patterned light sheets is capable of increasing the single-layer volume processing rate by at least three orders of magnitude; however, it still needs to be optimized to improve the manufacturing accuracy, and more importantly, to overcome the impact of proximity effect on printing quality.[29,30] The so-called "proximity effect" is the effect on the local photochemical environment of the nearby already exposed region, or the overlap of light energy near the writing point, or the heat or molecular diffusion near the writing point.[31–34] It is worth noting that parallel TPP processing techniques exhibit much more significant "proximity effect" than conventional single-point scanning due to the simultaneous exposure of a large number of adjacent voxels, which are challenging to overcome. Therefore, it is urgent to seek a universal TPP integration method that is efficient and high-resolution for wide range of fiber materials.

In this work, we developed a femtosecond laser hybrid 3D printing technology (FPL-DLW) by simultaneously including a DMD and a dual-axis galvanometer scanner in the optical system, which solves the difficulty of efficiently integrating high-precision 3D microstructures on the fiber tips. This FPL-DLW utilizes femtosecond projection lithography (FPL) to process the region with large volume and low resolution requirements, and direct laser writing (DLW) to produce the high-precision nanostructures that usually occupy a small volume fraction, making it suitable for various types of "Lab on Tip" devices. Here, two different coping strategies were devised according to the geometric shape of the fiber end devices: superposition combination and envelope combination. Finally, we demonstrated the efficient preparation of microlens arrays on fiber bundles and their direct application in optical imaging. The results verified the high resolution, high manufacturing throughput, high flexibility, and superior 3D processing capability of FPL-DLW. Briefly, for the first time to the best of our knowledge, we combined the fast on-demand continuous manufacturing function of FPL with the high resolution of DLW. This combination significantly improves the printing efficiency of TPP technology by up to two orders of magnitude; while, ensuring processing accuracy and pattern complexity, laying the foundation for the development of novel "all-in-fiber" devices that are accessible in various application scenarios.

2. Results and Discussion

2.1. FPL-DLW System

Figure 1a shows the optomechanical design of the FPL-DLW manufacturing system. The laser for FPL came from a femtosecond regenerative amplifier (Spectra-Physics Solstice Ace), with a central wavelength of 800 nm, pulse duration of 35 fs, and repetition rate of 1 kHz. By using a beam shaper (AdlOptica, πshaper 12_12), the Gaussian beam generated by the amplifier was converted into a flat-top beam; and then, uniformly covered all the pixels on the DMD panel. Lens L1 and a 60× water-immersion objective (Olympus, NA = 1.2) were used to reproduce the digital mask pattern loaded on the DMD at the focal plane of the objective. The seed laser (Spectra-Physics MaiTai SP, 800 nm, 60 nm bandwidth, 84 MHz) from another output port of the integrated amplifier was used for DLW. To control the movement of the laser focal point in the x–y direction, a dual-axis galvanometer was placed at the conjugation plane of the back aperture of the objective through a 4-f system (i.e., lens L1 and lens L2). Compared to the stage scanning system, the galvanometer-based DLW system not only had lower system costs and complexity but also offered sub-nanometer 3D positioning accuracy, extremely high scanning speed, and the ability for rapid focus jumping (<200 µs). A polarizing beam splitter (PBS) and two half-wave plates were employed to enable the same printing system to perform both FPL and DLW, based on the different polarization states of their respective light sources. This approach eliminated the need for repositioning and reduced time costs typically associated with using separate systems for these two modes. In addition, the advantage of this setup was that no adjustment of optical settings was required when switching between the two manufacturing modes, contributing to enhanced system stability. To facilitate in situ monitoring of the nanoscale manufacturing process, a microscopic imaging system was built in combination with the manufacturing device. This objective was shared between the imaging system and the manufacturing system. A charge-coupled device (CCD) camera positioned after the dichroic mirror recorded the manufacturing process. Samples used in the experiments, consisting of optical fibers with negative photoresist attached to their cleaved ends, were mounted on a motorized precision 3D translation stage.

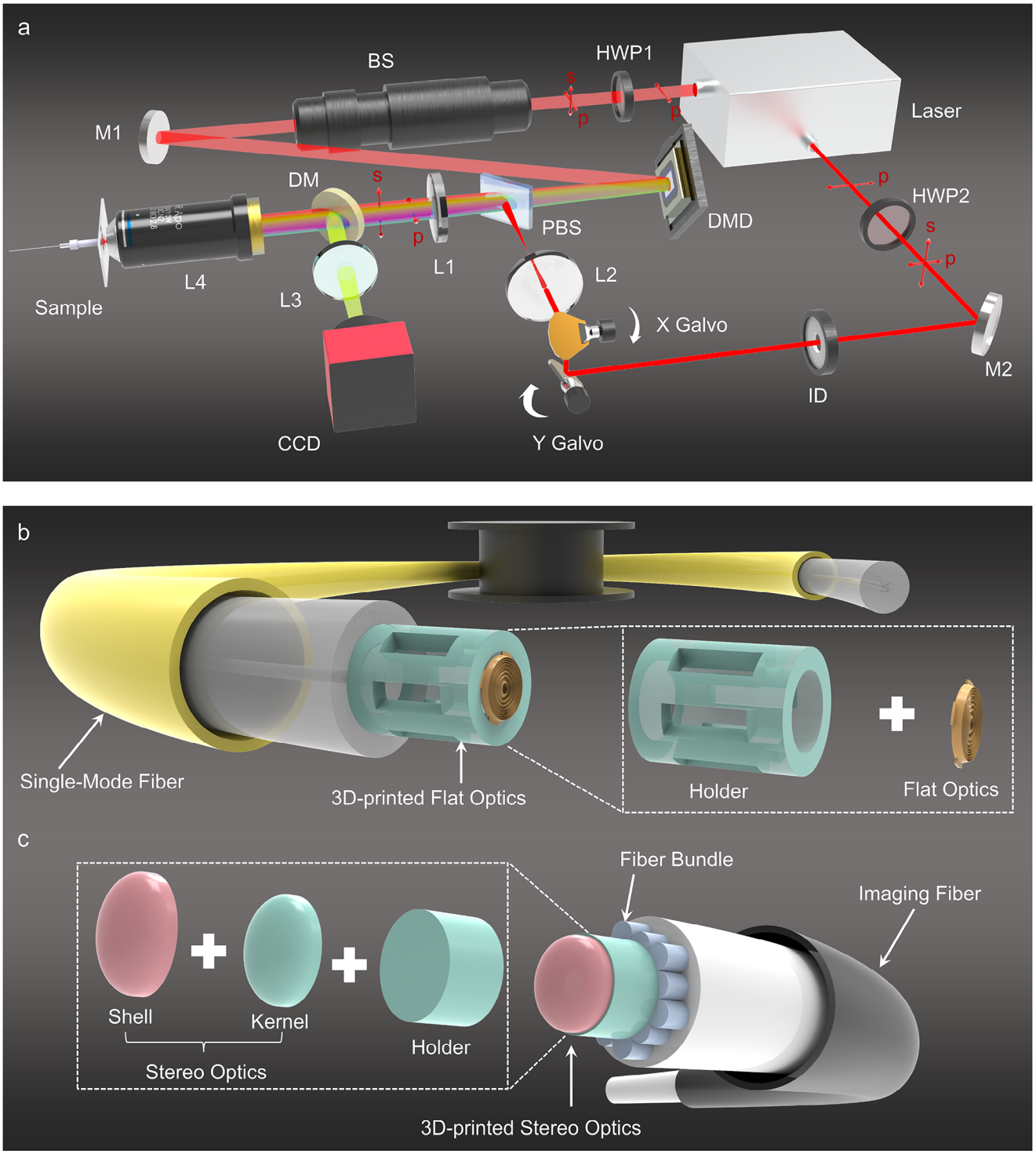

Figure 1. Configuration of the FPL-DLW system and segmentation methods of two typical fiber tip functional devices. a) Optomechanical setup of the FPL-DLW fabrication system. HWP, half wave plate; BS, beam shaper; M1 to M2, mirrors 1 to 2; DMD, digital micromirror device; PBS, polarizing beam splitter; L1 to L3, lenses 1 to 3; L4, objective lens; DM, dielectric mirror; CCD, charge-coupled device; ID, Iris diaphragm. b) Segmentation diagram of the flat optical device. c) Segmentation diagram of the stereo optical device.

2.2. Manufacturing Resolution of FPL-DLW System

The scanning step used in the fabrication process directly determines the processing quality and manufacturing time of the structures. Generally speaking, whether working with FPL or DLW, employing a larger scanning step can shorten the printing time, but the "staircase effect" on the structure surface is obvious; using a smaller scanning step can improve the surface quality, but the printing time will increase, resulting in a difficult trade-off between them. The users need to make a choice between printing accuracy and printing time or select a compromise resolution to process the entire structure. Therefore, it is crucial to select the appropriate resolution parameters by studying the quantitative relationship between the laser focusing conditions, including laser power and exposure time of a single light sheet or spot, and the feature sizes of FPL and DLW. Note that in the FPL-DLW hybrid approach, FPL is used to process large-volume holder or non-functional bulk inner structures, where its resolution does not affect the final "Lab on Tip" device. DLW is employed to finely process the surface nanostructures. Therefore, the manufacturing resolution of DLW directly determines the resolution of the hybrid system. For this purpose, we measured the resolution of SZ2080 negative photoresist printed under different exposure parameters in FPL (see Note S1, Supporting Information) and DLW (see Note S2, Supporting Information) systems. According to the measurement results, the minimum axial feature size of FPL printed single layer is ≈1 μm, and the minimum linewidth achieved by DLW is ≈170 nm. These results fully demonstrate the processing capabilities of the two subsystems and provide a basis for further rational structure segmentation.

2.3. Superposition Combination Strategy

It is crucial to reasonably split the 3D structure according to the fabrication capabilities of the two processing modules, which directly affects the overall fabrication efficiency and structure quality. We have classified the micro–optical devices into two categories according to their geometric structural characteristics: flat optical devices and stereo optical devices, as shown in Figure 1b,c. The optical functions of the former are derived from ultrathin planar layers, mainly including DOEs with "wavy" microstructures embedded in the materials,[35–38] metasurfaces composed of nanoscale scatterers arrays,[39–41] and suspended membranes for forming Fabry–Perot interferometers (FPI).[42,43] These devices usually require ultra-high substrates that are tens or even hundreds of times thicker than themselves to fix them at a specified position above the fiber end facet to achieve the set optical functions.[44–47] FPL can quickly prepare support structures with arbitrary cross-sectional shapes, but it is challenging to process fine planar optical components on the support base. FPL-DLW can use the arbitrary 3D processing capability of DLW to solve this difficulty. Essentially, FPL is employed to fabricate large volume supports with lower precision; while, DLW is utilized to craft ultra-thin, precision-critical light-modulating devices. These two processes are then combined to form a comprehensive structure. Based on this superposition combination manufacturing strategy, we experimentally created a multifocal diffractive lens (MfDL) owning a controllable intensity ratio on the SMF tip and characterized the focusing performance of this MfDL-enhanced fiber.

The wavefront $E(x, y)$ modulated by the diffractive lens satisfies the following equation:

$$E\ (x,y) = E_{\text{in}} \times H_{\text{lens}}\ (x,y) = E_{\text{in}} \times A_{\text{lens}} \cdot \exp\left(i\phi_{\text{lens}}\right) \tag{1}$$

$H_{\text{lens}}(x, y)$ is the transmission function of the lens, and A_{lens} and ϕ_{lens} are the amplitude and phase modulations of the lens, respectively. As the lens is used for wave phase retarding, the ϕ_{lens} is designed as:

$$\phi_{\text{lens}}\ (r) = -k_0\left(\sqrt{r^2+f^2}-f\right) \tag{2}$$

where k_0 is the free-space wave vector, r is the radial position of each phase component, and f is the focal length of the lens. For the conventional step-index SMF, when the transmission distance is significantly greater than the Rayleigh range, the SMF acts as a negative lens (**Figure 2a**) and exhibits its own spherical phase $\phi_{\text{fiber}} = k_0\ (\sqrt{r^2+l^2}-l)$ (l: propagation distance).[48] Therefore, consideration needs to be given to compensate this additional phase; so that, the focusing performance of the lens-enhanced fiber is optimized. The conversion of an on-fiber MfDL to the output light can be rewritten in more detail as follows:

$$H_{\text{MfDL}}\ (x,y) = \sum A_j \exp\left[i\left(-k_0\left(\sqrt{r^2+f_j^2}-f_j\right)-\phi_{\text{fiber}}\right)\right] \tag{3}$$

where A_j is the normalized amplitude constant corresponding to focal j, and f_j refers to axial coordinate of foci j. The phase profile of the on-fiber MfDL obtained after wavefront correction is expressed as:

$$\varphi\ (x,y) = \text{angle}\left[H_{\text{MfDL}}\ (x,y)\right] \text{modulo}\ 2\pi \tag{4}$$

With the help of the above design principle, we designed the MfDL with two focal points on the SMF end face. The designed values for f_1 and f_2 were 53 and 63 μm, respectively. We controlled their relative intensity by changing the ratio between A_1 and A_2. Figure 2b provides the phase distribution of the MfDL with equal focusing intensities at two coaxial spots.

Figure 2c illustrates the processing process of the superposition combination form. In the first step, FPL printed a hollow cylindrical base with a height of 150 μm, a diameter of 92 μm, and a sidewall thickness of 23 μm onto the end face of the SMF (Figure 2d) to expand its output in free-space and took 24 s (the processing time used by FPL is calculated under the following conditions: the exposure time of each layer is 160 ms, and the layer space is 1 μm) (see Note S3, Supporting Information). In the second step, the MfDL was precisely positioned above the SMF end face using DLW (Figure 2e), which took 12 min and 14 s. As is well known, the DOE imparts required phase delay on the incident radiation by changing the height of each unit along the optical axis. For MfDL, the conversion relationship between the height h of the diffraction unit and the phase φ of the corresponding pixel point on the phase map satisfies $h = \lambda\varphi/[2\pi(n-1)]$, where λ represents the working wavelength and n represents the refractive index of the material. In this step, the optimized printing parameters were 100 nm and 6 mW for the scanning step and

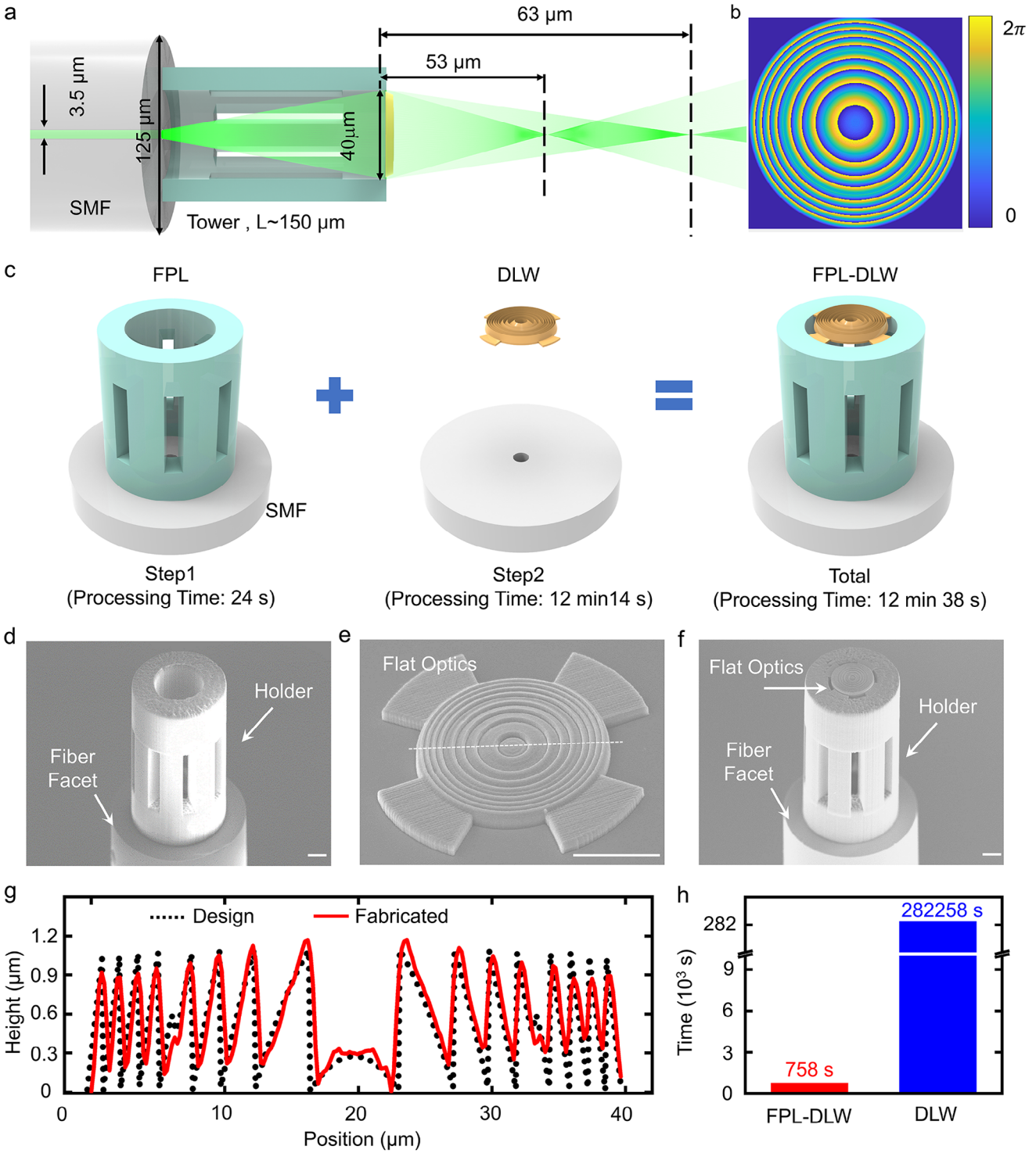

Figure 2. Design, fabrication, and characterization of the on-fiber MfDL. a) Detailed view of the multi-focus fibre consisting of an SMF, the hollow tower structure for beam expansion, and the MfDL on its facet. b) Phase pattern of the on-fiber MfDL with the intensity ratio of two coaxial spots taking 1:1 wrapped between 0 and 2π. Size, 400×400 pixels. c) 3D schematic diagram of the processing process. d) SEM micrograph of the hollow tower processed by FPL. e) SEM micrograph of the MfDL processed by DLW. f) SEM micrograph of the MfDL-enhanced fiber obtained by superposition combination strategy. g) Height profile with respect to the substrate (3 μm) along the white line shown in (e). h) Comparison of the processing time of the on-fiber MfDL prepared using the FPL-DLW and the DLW. All scale bars: 20 μm.

laser power, respectively. In our work, to achieve rapid direct laser writing, the exposure time on a single point was fixed at 400 µs. Scanning electron microscope (SEM) images verify that the designed MfDL was successfully fabricated on the hollow tower-like holder (Figure 2f). To further characterize the surface morphology, the radial surface profile of the MfDL was measured using an atomic force microscope (AFM). The results show a good match between the designed profile and the actual fabricated profile (Figure 2g). More importantly, for MfDL-enhanced fiber, using DLW to process the entire structure required a manufacturing time of ≈78.4 h (the scanning step and laser power were 100 nm and 6 mW, respectively); while, the superposition combination method only took 12 min and 38 s (Figure 2h). The above experimental results verified the high manufacturing throughput and the precision fabrication ability of the superposition combination strategy, which was proposed for on-fiber flat optical devices.

The performance of the MfDL-enhanced fiber was characterized by coupling light from a semiconductor laser source operating at 532 nm into the fiber sample. As shown in **Figure 3**d, the emerging beam from the fiber underwent expansion within the hollow tower structure, ultimately reaching the size of the lens and achieving the anticipated wavefront manipulation. A homemade microscopic imaging system with z-translation capabilities was used to collect the transverse beam profile at different axial positions, which allowed the characterization of the image plane field profile as a function of distance along the z-axis. Figure 3a shows the theoretical intensity distribution along the axis of propagation, normalized relative to its maximum value. It is not surprising that two spots with the same peak intensity corresponding to the two foci f_1 and f_2 are observed. Figure 3b shows the normalized intensity distribution measured in the x–z plane. The analysis was achieved by combining a series of images sampled parallel to the MfDL plane; while, scanning the z-axis with a step of 1 µm. The red and blue curves in Figure 3c are 1D intensity distributions extracted from the 2D simulation and measurement results along the optical axis, respectively. The measurement results are in good agreement with the simulation results, which proves the validity of the proposed method. More details are shown in Figure 3f, which reports the experimental measurement intensity distributions at positions 48, 53, 58, 63, and 68 µm away from the MfDL surface, marked by $z_1 - z_5$. The simulated intensity distribution (Figure 3e) was consistent with the experimental observation. This innovative multifocal fiber presents an exciting development as it allows for customization of the number, longitudinal position, and intensity ratio of focal spots to cater to specialized requirements. Its potential applications span across particle manipulation, imaging, and quantum information processing, effectively contributing to the reduction in size of photonic systems.

2.4. Envelope Combination Strategy

Comparatively, in stereo optical devices,[49] their performance is predominantly determined by the 3D topography of the external profile, and the voxels inside the structure do not contribute to the surface quality but occupy a considerable proportion of the device volume, such as free-form lenses with a single refractive surface, reflecting elements exploiting curved mirror surfaces, as well as more complex structures, including high-performance multi-lens assemblies. Shell-scanning TPP is an ideal solution to improve the processing efficiency of such devices.[50,51] However, thin surface layers can cause the structure to collapse and deform during development.[52] Solving this problem by increasing the surface layer thickness inevitably reduces the processing efficiency. Given that the internal filling of a stereo optical device does not require high precision, we use FPL to process the interior and DLW to refine the surface, which is called envelope combination. To study the effect of envelope combination strategy, we designed and fabricated an aspheric microlens with a diameter of 100 µm and a height of 26 µm. The designed asphere satisfied the following equation:

$$Z(r) = cr^2 / \left[1 + \sqrt{1 - (1+k)\,c^2 r^2}\right] + \sum_{i=1}^{8} a_i r^{2i} \tag{5}$$

Here, c is the curvature, k is the conic constant, r is the radial distance measured from the optical axis, and a_i describes the surface deviation from the axially symmetric quadric surface specified by c and k. a_i and k provide additional degrees of freedom to compensate for aberrations compared to spherical surfaces commonly used in traditional lens design. An 8-order even aspherical surface was used in this work.

The surface layer of the aspheric microlens consisted of a dense nanoshell (thickness: 400 nm) and a buffer layer (thickness: 1.2 µm), which overlapped with the structure inside to ensure the bonding strength between the surface and the interior. The preparation process is illustrated in **Figure 4**a. In the first step, FPL was used to perform the inner filling in less than 2 s (Figure 4b). Here, a slice interval of 500 nm, a single-layer exposure time of 40 ms, and a laser power of 60 mW were applied in our projection exposure (see Note S5, Supporting Information). The steps generated by layering were flattened by self-smoothing effect.[50] In the second step, a large scanning step (300 nm) and a high-power femtosecond laser (laser power: 10 mW) were chosen to efficiently scan the buffer layer; while, a small scanning step (100 nm) and a low-power femtosecond laser (laser power: 6 mW) were employed to accurately define the nanoshell (Figure 4c), which took a total time of 35 min and 4 s. To verify the high manufacturing throughput and precision machining ability of FPL-DLW, the same lens was processed using DLW. The radial profiles of the two lenses were measured by a laser confocal microscopy (LSCM), and Figure 4e shows that the measured values of the two lenses were basically consistent with the theoretical design. These results have shown that the surface quality of the lens created by FPL-DLW was the same as the one fabricated directly by DLW. While DLW took over 23.7 h to complete, FPL-DLW took only 35 min and 6 s. In addition, the measured intensity distribution of the sample prepared by hybrid processing and the beam cut-profiles along the symmetry axes of the focus are reported in Figure 4f–h.

The quality of optical imaging determines the practical value of aspherical lenses. **Figure 5**a illustrates the setup of the microscopic imaging system. Illumination light was provided by an light-emitting diode (LED) with a wavelength of 528 nm. To enhance illumination, a condenser lens was placed in front of the imaging target. The images generated by the aspheric lens

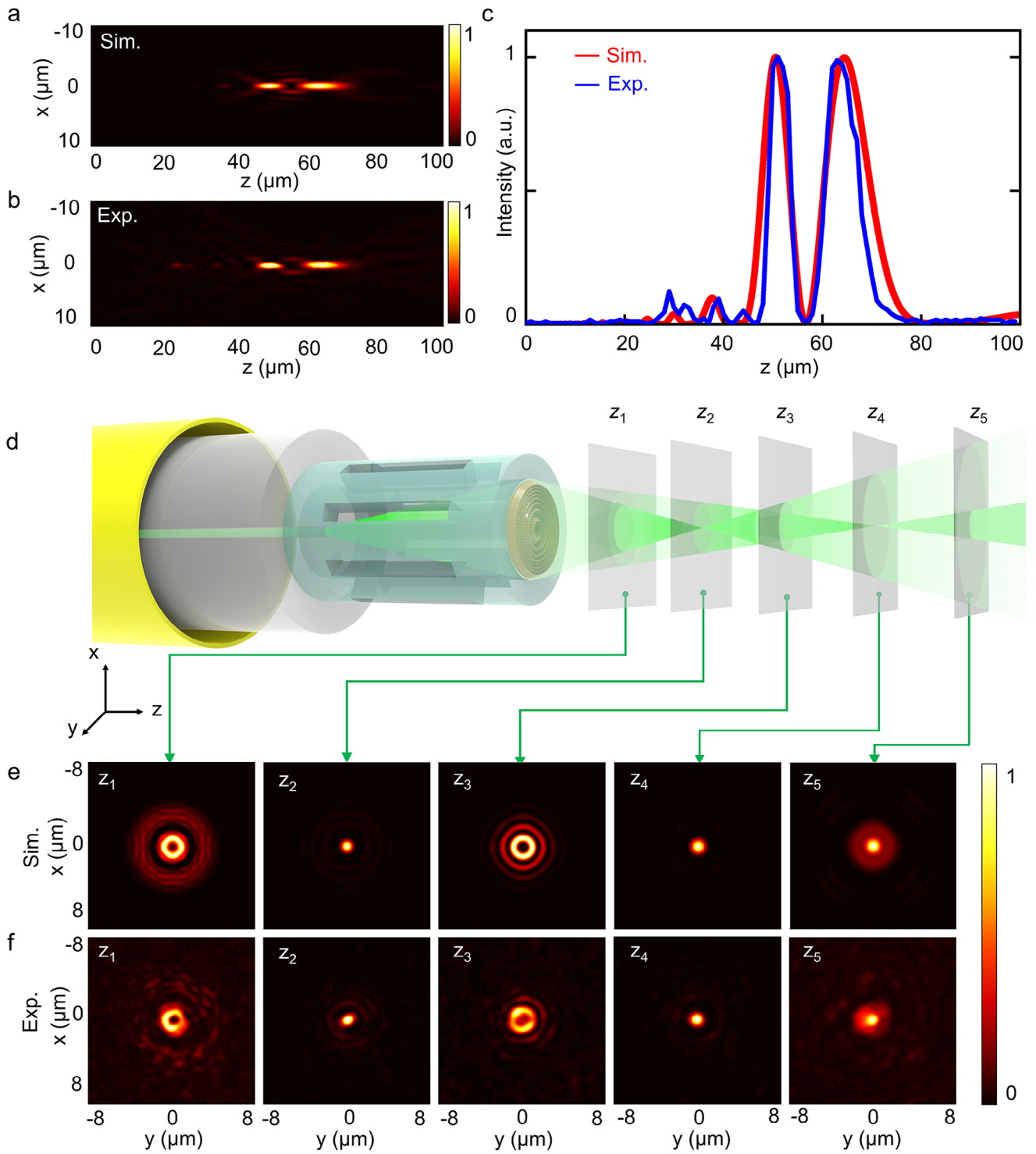

Figure 3. Simulated and measured focusing performance of the on-fiber MfDL. a) Simulated and b) measured intensity profiles along the focusing *x*–*z* plane normalized with respect to its maximum. c) The intensity cut-profile of the normalized maps (a,b) as a function of the optical axis *z*. d) Schematic of the focusing performance of the on-fiber MfDL when illuminated by a fully extended beam at normal incidence. e) Images of the intensity distributions simulated at various locations on the optical axis. The mutual distance between the planes is 5 μm, starting from the plane near the MfDL (from left to right). The two focal planes are located at $z_2 = 53$ and $z_4 = 63$ μm respectively. f) Measured intensity distributions with the same 5 μm spacing along the optical axis.

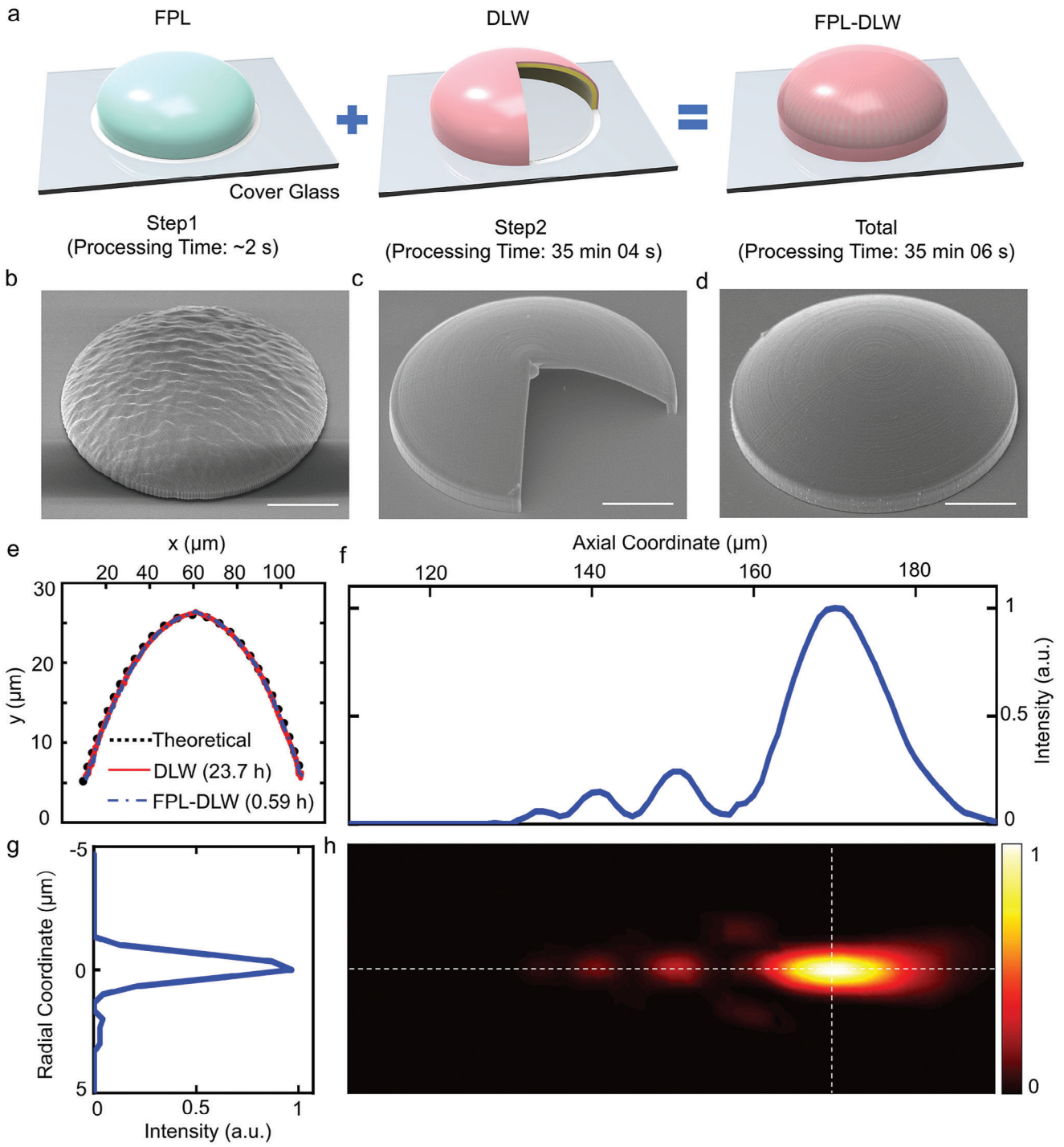

Figure 4. Fabrication and characterization of the aspheric microlens. a) 3D schematic diagram of the processing process. b) SEM micrograph of the inner core processed by FPL. c) SEM micrograph of the surface layer processed by DLW. d) SEM micrograph of the aspheric microlens obtained by envelope combination form. e) Contour contrast diagram. f) Axial and g) radial intensity profiles along the symmetry axes of the focus. h) Measured focal spot of the microlens. All scale bars: 25 μm.

were captured using a microscope system, which consisted of an objective lens, a lens, and a CCD camera. The optical resolution of the aspheric microlenses processed by DLW and FPL-DLW was tested using a United States Air Force (USAF) 1951 resolution chart. The magnified optical microscope photo of the used USAF 1951 is shown in Figure 5b. Figure 5c,d are images of the patterns in group 6 observed by the two microlenses, and the inset graphs show the intensity contrast between adjacent line elements measured along the dashed lines. The results show that both aspheric lenses can clearly distinguish up to element

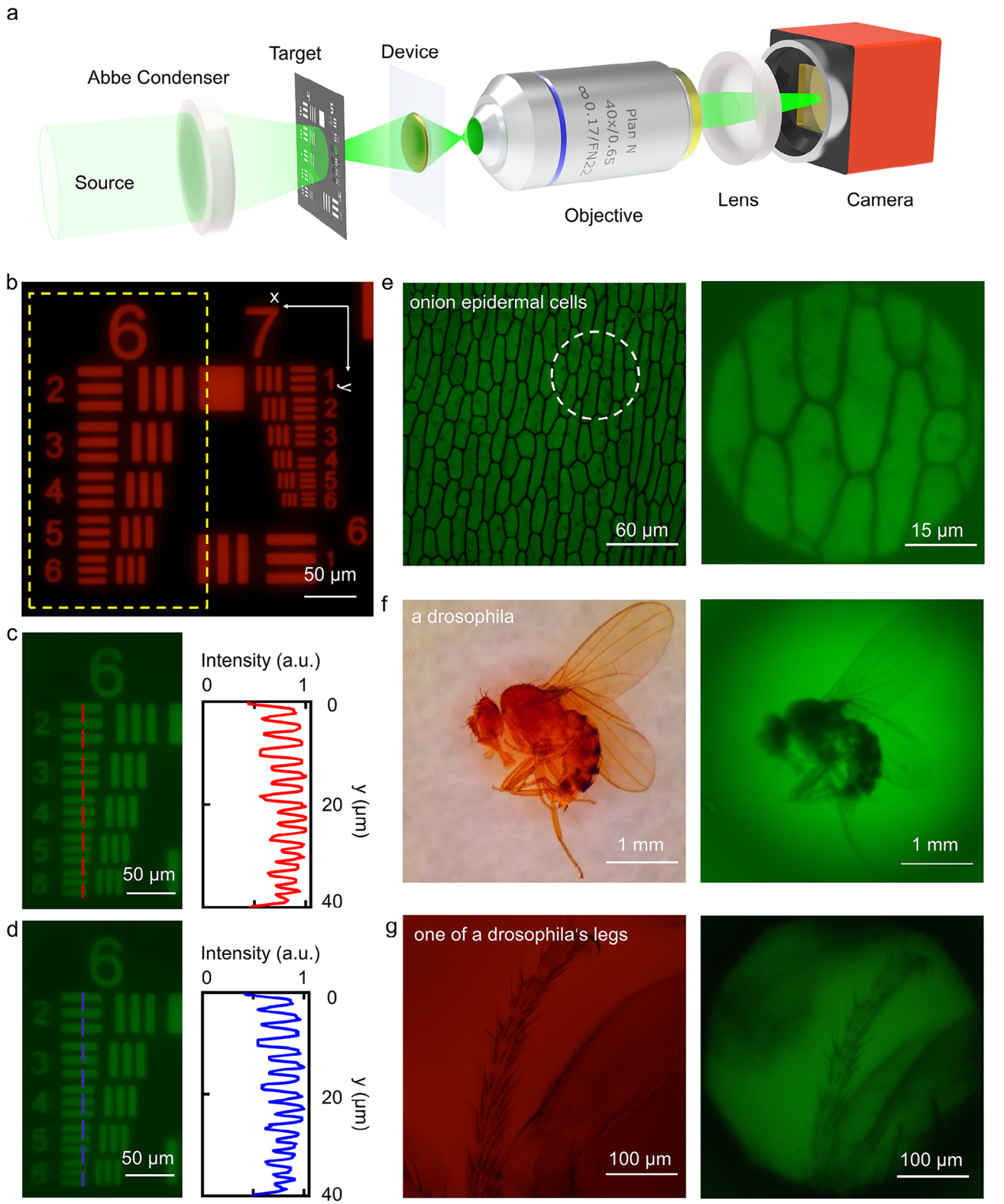

Figure 5. Imaging behaviors of the fabricated aspheric microlenses. a) Experimental optical setup used for measuring the imaging properties of the fabricated aspheric lenses. b) The optical microscope image of USAF 1951 resolution chart. c,d) Microscopic images of the resolution target selected part in (b) obtained by microlenses processed using the FPL-DLW and the DLW, respectively. The inset graphs are intensity contrast between adjacent line elements measured along the dashed lines. Microscopic images of e) onion epidermal cells, f) a drosophila, and g) one of its legs, which were captured using an optical microscope (left) and a lens processed by hybrid processing (right), respectively.

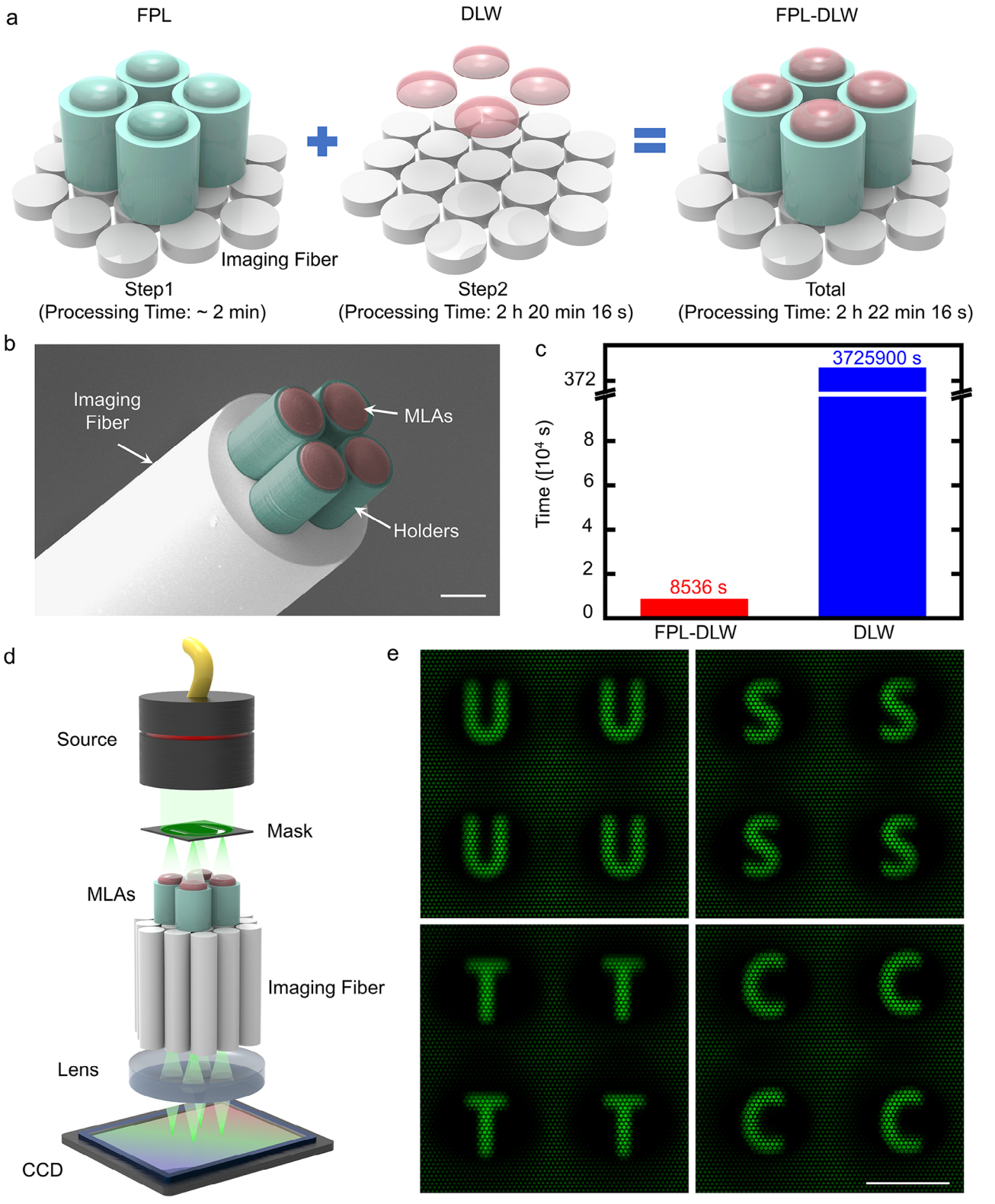

Figure 6. A square array of four microlenses printed directly on an imaging fiber by FPL-DLW. a) 3D schematic diagram of the processing process. b) SEM image of one array of four microlenses symmetrically set in a square configuration on the fiber end. c) Comparison of processing times between using the FPL-DLW and the DLW approaches of the MLAs. d) Schematic diagram of the imaging testing system. e) Square image arrays of the negative masks with letters "U," "S," "T," and "C" obtained under transmitted light illumination. Scale bars: 100 μm.

6 (line pair: 80 LP/mm, linewidth: 5 μm). In addition, to verify the imaging effect of the aspheric lens prepared by the envelope combination form on biological samples, we performed imaging tests on onion epidermal cells, a drosophila and one of its legs, presenting the expected superior imaging results (Figure 5e–g). This envelope combination strategy provides a promising path for the mass manufacturing of higher-performance stereo optical devices, resembling the above-mentioned aspheric microlens integrated onto the fiber end faces.

2.5. Integration of Two Composite Strategies

To further verify the high precision, high efficiency, and arbitrary 3D processing capability of FPL-DLW, one array of four aspheric lenses symmetrically set in a square was printed on the end facet of an imaging fiber. **Figure 6a** provides an overview of the processing steps. In the first step, FPL machined the bottom 2 × 2 array structure, which consisted of 2 × 2 cylinders measuring 170 μm in height and 120 μm in diameter, and a 2 × 2 inner core of the microlenses array. In the second step, DLW was used to cover the outer surfaces of these four lenses. The whole process took only ≈143 min, of which FPL accounted for 2 min and DLW for 141 min; while, using DLW directly to process the entire structure required more than 43 days (Figure 6c). Figure 6b shows the SEM image of the array of four microlenses printed onto the end face of an imaging fiber. The experimental device for testing the optical performance of the on-fiber microlens arrays (MLAs) is depicted in Figure 6d. Each microlens had an image area diameter of about 100 μm, and each encompassed ≈700 pixels of the imaging fiber. As the pixel diameter of each pixel was 4 μm, the resolution was limited by this specific fiber geometry. Figure 6e shows the test results obtained from the on-fiber MLAs under transmitted light illumination. The square image arrays of the negative masks with letters "U," "S," "T," and "C" were clearly recognizable. This FPL-DLW technology has presented a cost-effective roadmap for mass production of fiber-coupled MLAs, which may find applications in the rapid proliferating optical communication, optical sensing, and biomedicine. Currently, DLW equipments on the market for TPP integration of fiber tip devices have done quite well, such as Nanoscribe's two-photon grayscale lithography (2GL) technology.[53] We have ample reason to believe that the FPL-DLW hybrid strategy can help them achieve faster processing speeds than they already do (see Note S8, Supporting Information).

3. Conclusion

In summary, we proposed a method that combined femtosecond projection lithography and direct laser writing to fabricate complex 3D micro–optical structures on fiber tips. Projection exposure was used for the bases or interior structures with large volumes and low precision requirements; while, direct laser writing was used for the fine flat optical devices or smooth surfaces of stereo optical devices. By using PBS to reflect or transmit beams with different polarization characteristics from two subsystems, patterned exposure and direct laser writing could be flexibly switched without increasing the complexity of the optical system. The FPL-DLW inherited the advantages of high efficiency from FPL and high precision from DLW to achieve the processing of the "Lab on Tip" devices, such as the MfDL on the tip of the SMF and aspheric microlens arrays at the imaging fiber end. The good structure quality and extremely short processing time proved the superiority of FPL-DLW technology. We anticipate that the formidable processing capabilities of FPL-DLW can play a pivotal role in advancing the integration of materials and structures on the tips of various fibers, leading to increased yields. This, in turn, opens up new opportunities for the development of commercialized all-fiber systems tailored for applications in life sciences, clinical research, medical testing, and diagnosis.

4. Experimental Section

Sample Preparation and Fabrication: First, a home-made support tube was used to hold the optical fiber in a vertical orientation and maintain a gap between the fiber end and the cover glass of > 200 μm. Next, 10 μL of photoresist (SZ2080, IESL-FORTH) was dropped on the glass substrate to wrap the fiber tip and prebaked at 100 °C for 1 h to evaporate the solvent in the SZ2080. Then, the fiber was suspended with the tip facing downward toward the focal plane of the processing system. The position of the fiber was adjusted according to a magnified CCD image under transmitted light illumination. After that, the designed structure was directly printed on the far end of the fiber by FPL-DLW. After polymerization, the sample was developed in 1-propanol for 30 min until all unpolymerized photoresist was washed off.

Sample Characterization: The SEM images were taken with a secondary electron scanning electron microscope (ZEISS EVO18) operated at an accelerating voltage of 10 keV with a working distance of 8 mm after depositing ≈ 10 nm of gold. The topography of the MfDL was scanned at a rate of 0.5 Hz in air in tapping mode with a commercial AFM (Dimension Icon, Bruker, CA) using a PPP-FM probe (NANOSENSORS, Switzerland). The surface profiles of aspheric microlenses were captured by an LSCM (ZEISS LSM900).

Supporting Information

Supporting Information is available from the Wiley Online Library or from the author.

Acknowledgements

This work was supported by the National Key Research and Development Program of China (Nos. 2024YFB4610700, 2021YFF0502700), the National Natural Science Foundation of China (Nos. 62325507, 52375582, 61927814, 52122511, and 62475252), the Major Scientific and Technological Projects in Anhui Province (202203a05020014), the National Science Foundation of Anhui (2408085MF151) and the CAS Project for Young Scientists in Basic Research (No.YSBR-049). The authors acknowledge the Experimental Center of Engineering and Material Sciences at USTC for the fabrication and measuring of samples. This work was partly carried out at the USTC Center for Micro and Nanoscale Research and Fabrication. The authors thank Chengfu Ma for AFM imaging and Wei Li for LSCM imaging.

Conflict of Interest

The authors declare no conflict of interest.

Author Contributions

L.X. and Y.X. contributed equally to this work. L.X., Y.X., C.W., D.W., and Y.H. conceived the idea and designed the project. L.X., Y.X., C.W., X.G., Y.T., and X.W. performed all the experiments. L.X., C.W., C.Z., Li.Z., and Le.Z. performed the characterization. L.X. and X.G. performed the simulation. L.X., Y.X., C.W., Y.T., and X.W. completed data analysis and figure depicture. L.X., C.W., and D.W. wrote and revised the paper. C.W., J.L., D.W., J.C., and Y.H. supervised the project.

Data Availability Statement

The data that support the findings of this study are available from the corresponding author upon reasonable request.

Keywords

direct laser writing, fiber tip devices, hybrid 3D processing, projection lithography

Received: May 16, 2024
Published online:

[1] P. Vaiano, B. Carotenuto, M. Pisco, A. Ricciardi, G. Quero, M. Consales, A. Crescitelli, E. Esposito, A. Cusano, *Laser Photonics Rev.* **2016**, *10*, 922.
[2] Y. Liang, W. Fu, Q. Li, X. Chen, H. Sun, L. Wang, L. Jin, W. Huang, B.-O. Guan, *Nat. Commun.* **2022**, *13*, 7604.
[3] D. Liu, Z. Cai, B. Li, M. Zou, L. Zhang, Y. Hua, J. Mai, C. Zhao, C. Liao, J. He, X. Weng, L. Liu, J. Qu, Y. Wang, *Opt. Express* **2023**, *31*, 2207385.
[4] Ó. Esteban, F. B. Naranjo, N. Díaz-Herrera, S. Valdueza-Felip, M.-C. Navarrete, A. González-Cano, *Sens. Actuators, B* **2011**, *158*, 372.
[5] F. Piccirillo, M. Giaquinto, A. Ricciardi, A. Cusano, *Results in Optics* **2022**, *6*, 100203.
[6] Q. Zhao, W. Yuan, J. Qu, Z. Cheng, G.-D. Peng, C. Yu, *Nanomaterials* **2022**, *12*, 793.
[7] J. E. Fröch, L. Huang, Q. a. A. Tanguy, S. Colburn, A. Zhan, A. Ravagli, E. J. Seibel, K. F. Böhringer, A. Majumdar, *eLight* **2023**, *3*, 13.
[8] X. Sun, Z. Lei, H. Zhong, C. He, S. Liu, Q. Meng, Q. Liu, S. Chen, X. Kong, T. Yang, *Light Adv. Manuf.* **2022**, *3*, 665.
[9] G. Kostovski, P. R. Stoddart, A. Mitchell, *Adv. Mater.* **2014**, *26*, 3798.
[10] Y. Xiong, F. Xu, *Adv. Photonics* **2020**, *2*, 064001.
[11] C. Xiong, C. Liao, Z. Li, K. Yang, M. Zhu, Y. Zhao, Y. Wang, *Front. Mater.* **2020**, *7*, 586496.
[12] C. Xin, L. Yang, J. Li, Y. Hu, D. Qian, S. Fan, K. Hu, Z. Cai, H. Wu, D. Wang, D. Wu, J. Chu, *Adv. Mater.* **2019**, *31*, 1808226.
[13] C. Wang, Z. Hu, L. Yang, C. Zhang, L. Zhang, S. Ji, L. Xu, J. Li, Y. Hu, D. Wu, J. Chu, K. Sugioka, *Opt. Lett.* **2021**, *46*, 2968.
[14] B. Dong, B. Liu, C. Chen, D. Wang, L. Zhang, L. Xu, W. Xiong, J. Li, Y. Hu, J. Chu, D. Wu, *Opt. Lett.* **2023**, *48*, 2508.
[15] C. Xin, Z. Ren, L. Zhang, L. Yang, D. Wang, Y. Hu, J. Li, J. Chu, L. Zhang, D. Wu, *Nat. Commun.* **2023**, *14*, 4273.
[16] T. Gissibl, S. Thiele, A. Herkommer, H. Giessen, *Nat. Photonics* **2016**, *10*, 554.
[17] T. Gissibl, S. Thiele, A. Herkommer, H. Giessen, *Nat. Commun.* **2016**, *7*, 11763.
[18] M. Power, A. J. Thompson, S. Anastasova, G. Z. Yang, *Small* **2018**, *14*, 1703964.
[19] S. Zhang, S. J. Tang, S. Feng, Y. F. Xiao, W. Cui, X. Wang, W. Sun, J. Ye, P. Han, X. Zhang, Y. Zhang, *Adv. Opt. Mater.* **2019**, *7*, 1900602.
[20] J. A. Kim, D. J. Wales, A. J. Thompson, G. Z. Yang, *Adv. Opt. Mater.* **2020**, *8*, 1901934.
[21] A. Bertoncini, C. Liberale, *Optica* **2020**, *7*, 1487.
[22] S. Schmidt, S. Thiele, A. Toulouse, C. Bösel, T. Tiess, A. Herkommer, H. Gross, H. Giessen, *Optica* **2020**, *7*, 1279.
[23] J. Li, S. Thiele, B. C. Quirk, R. W. Kirk, J. W. Verjans, E. Akers, C. A. Bursill, S. J. Nicholls, A. M. Herkommer, H. Giessen, R. A. Mclaughlin, *Light: Sci. Appl.* **2020**, *9*, 100203.
[24] L. Xu, C. Wang, X. Qi, R. Li, C. Zhang, L. Zhang, Z. Ren, Z. Zhang, J. Li, Y. Hu, D. Wu, J. Chu, *Appl. Phys. Lett.* **2021**, *119*, 131101.
[25] J.-I. Kato, N. Takeyasu, Y. Adachi, H.-B. Sun, S. Kawata, *Appl. Phys. Lett.* **2005**, *86*, 044102.
[26] V. Hahn, P. Kiefer, T. Frenzel, J. Qu, E. Blasco, C. Barner-Kowollik, M. Wegener, *Adv. Funct. Mater.* **2020**, *30*, 1907795.
[27] Y. Hu, W. Feng, C. Xue, Z. Lao, S. Ji, Z. Cai, W. Zhu, J. Li, D. Wu, J. Chu, *Opt. Lett.* **2020**, *45*, 4698.
[28] L. Zhang, B. Liu, C. Wang, C. Xin, R. Li, D. Wang, L. Xu, S. Fan, J. Zhang, C. Zhang, Y. Hu, J. Li, D. Wu, L. Zhang, J. Chu, *Nano Lett.* **2022**, *22*, 5277.
[29] S. K. Saha, D. Wang, V. H. Nguyen, Y. Chang, J. S. Oakdale, S.-C. Chen, *Science* **2019**, *366*, 105.
[30] P. Somers, Z. Liang, J. E. Johnson, B. W. Boudouris, L. Pan, X. Xu, *Light: Sci. Appl.* **2021**, *10*, 199.
[31] C. Arnoux, L. A. Pérez-Covarrubias, A. Khaldi, Q. Carlier, P. L. Baldeck, K. Heggarty, A. Banyasz, C. Monnereau, *Addit. Manuf.* **2022**, *49*, 102491.
[32] H. Kim, R. Pingali, S. K. Saha, *Virtual Phys. Prototyping* **2023**, *18*, e2230979.
[33] L. Pérez Covarrubias, C. Arnoux, Q. Carlier, A. Khaldi, P. Baldeck, K. Heggarty, Proc. of SPIE Vol, **2020**, *11349*, 113490O-1.
[34] S. K. Saha, C. Divin, J. A. Cuadra, R. M. Panas, *J. Micro Nano Manuf.* **2017**, *5*, 031002.
[35] T. Gissibl, M. Schmid, H. Giessen, *Optica* **2016**, *3*, 448.
[36] K. Weber, F. Hütt, S. Thiele, T. Gissibl, A. Herkommer, H. Giessen, *Opt. Express* **2017**, *25*, 19672.
[37] N. Lassaline, R. Brechbühler, S. J. W. Vonk, K. Ridderbeek, M. Spieser, S. Bisig, B. Le Feber, F. T. Rabouw, D. J. Norris, *Nature* **2020**, *582*, 506.
[38] W. A. Britton, Y. Chen, F. Sgrignuoli, L. Dal Negro, *Laser Photonics Rev.* **2021**, *15*, 2000207.
[39] X. Chen, M. Chen, M. Q. Mehmood, D. Wen, F. Yue, C. W. Qiu, S. Zhang, *Adv. Opt. Mater.* **2015**, *3*, 1201.
[40] S. Zhang, P. Huo, W. Zhu, C. Zhang, P. Chen, M. Liu, L. Chen, H. J. Lezec, A. Agrawal, Y. Lu, T. Xu, *Laser Photonics Rev.* **2020**, *14*, 2000062.
[41] C. Xin, Z. Ren, L. Zhang, L. Yang, D. Wang, Y. Hu, J. Li, J. Chu, L. Zhang, D. Wu, *Nat. Commun.* **2023**, *14*, 4273.
[42] M. Zou, C. Liao, S. Liu, C. Xiong, C. Zhao, J. Zhao, Z. Gan, Y. Chen, K. Yang, D. Liu, Y. Wang, Y. Wang, *Light: Sci. Appl.* **2021**, *10*, 171.
[43] C. Liao, C. Xiong, J. Zhao, M. Zou, Y. Zhao, B. Li, P. Ji, Z. Cai, Z. Gan, Y. Wang, Y. Wang, *Light Adv. Manuf.* **2022**, *3*, 3.
[44] W. Hadibrata, H. Wei, S. Krishnaswamy, K. Aydin, *Nano Lett.* **2021**, *21*, 2422.
[45] I. V. a. K. Reddy, A. Bertoncini, C. Liberale, *Optica* **2022**, *9*, 645.
[46] H. Ren, J. Jang, C. Li, A. Aigner, M. Plidschun, J. Kim, J. Rho, M. A. Schmidt, S. A. Maier, *Nat. Commun.* **2022**, *13*, 4183.
[47] M. Zou, C. Liao, Y. Chen, L. Xu, S. Tang, G. Xu, K. Ma, J. Zhou, Z. Cai, B. Li, C. Zhao, Z. Xu, Y. Shen, S. Liu, Y. Wang, Z. Gan, H. Wang, X. Zhang, S. Kasas, Y. Wang, *Int. J. Extreme Manuf.* **2023**, *5*, 015005.
[48] M. Plidschun, H. Ren, J. Kim, R. Förster, S. A. Maier, M. A. Schmidt, *Light: Sci. Appl.* **2021**, *10*, 57.
[49] P. I. Dietrich, M. Blaicher, I. Reuter, M. Billah, T. Hoose, A. Hofmann, C. Caer, R. Dangel, B. Offrein, U. Troppenz, M. Moehrle, W. Freude, C. Koos, *Nat. Photonics* **2018**, *12*, 241.
[50] D. Wu, S.-Z. Wu, L.-G. Niu, Q.-D. Chen, R. Wang, J.-F. Song, H.-H. Fang, H.-B. Sun, *Appl. Phys. Lett.* **2010**, *97*, 031109.
[51] M. Marini, A. Nardini, R. Martínez Vázquez, C. Conci, M. Bouzin, M. Collini, R. Osellame, G. Cerullo, B. S. Kariman, M. Farsari, E. Kabouraki, M. T. Raimondi, G. Chirico, *Adv. Funct. Mater.* **2023**, *33*, 2213926.
[52] D. Wu, J. Xu, L.-G. Niu, S.-Z. Wu, K. Midorikawa, K. Sugioka, *Light: Sci. Appl.* **2015**, *4*, e228.
[53] L. Siegle, S. Ristok, H. Giessen, *Opt. Express* **2023**, *31*, 4179.